Proceedings of the ASME 37nd International Conference on Ocean, Offshore and Arctic Engineering
OMAE2018
June 17-22, 2018, Madrid, Spain

OMAE2018-77534

RESONANT STEADY-STATE SLOSHING IN UPRIGHT TANKS: EFFECT OF THREE-DIMENSIONAL EXCITATIONS AND VISCOSITY

Alexander N. Timokha
Centre for Autonomous Marine Operations and Systems (AMOS)
Department of Marine Technology
Norwegian University of Science and Technology
Trondheim, Norway

Ihor A. Raynovskyy
Institute of Mathematics
National Academy of Sciences of Ukraine
Kiev, Ukraine

ABSTRACT

Bearing in mind recent experimental and theoretical results showing that the viscous damping can qualitatively affect the resonant sloshing in clean tanks, the Narimanov-Moiseev multimodal sloshing theory for an upright circular container is revised to analytically construct and analyze the steady-state surface waves when the container performs a small-amplitude sway/roll/pitch/surge prescribed periodic motion with the forcing frequency close to the lowest natural sloshing frequency. The revised theory is applicable for the radius-scaled mean liquid depths $h>1$ providing the secondary resonance phenomena do not occur at the primary resonance zone. A focus is on how the damping influences the phase lag as well as on the amplitude response curves versus the forcing type, which can in the lowest-order approximation be treated as if the container translatory moves along an elliptic orbit in the horizontal plane. The analytical results are compared with existing experiments for longitudinal and circular orbital tank excitations. Whereas a good agreement is found for the longitudinal excitation, a discrepancy is detected for the circular orbital forcing. The discrepancy may, most probably, be explained by the wave breaking and the steady rotational flow (Ludwig Prandtl, 1949) phenomena. Occurrence of the Prandtl flow makes inapplicable the existing analytical inviscid sloshing theories, even if they are modified to account for the damping. New ideas on how to construct an appropriate analytical viscous sloshing theory are required.

INTRODUCTION

Resonant nonlinear sloshing and associated hydrodynamic loads occurring due to *three-dimensional* excitations of a clean (no submerged structures) cylindrical tanks is of concern for ship and offshore storage applications. Typically, the liquid sloshing dynamics is either *analytically* studied to classify the steady-state waves (the frequency domain problem) or *numerically* simulated by adopting a CFD solver to describe wave transients with different initial scenarios (the time domain problem). Whereas the modern solvers most often adopt the viscous hydrodynamic model with either no-slip or Navier's or frictionless boundary conditions on the wetted tank surface, the analytical studies suggest an inviscid incompressible liquid with irrorational flows. This means that the existing analytical approaches neglect viscous and vortex phenomena in clean tanks. Even being so, they provide a rather accurate (chaps. 8-9 of [1]) steady-state prediction, at least, for the finite liquid depth and resonant excitations of the lowest natural sloshing frequency. A satisfactory agreement with experiments was established for wave elevations, resulting hydrodynamic force and moment when tank is exposed to the prescribed harmonic forcing in a symmetry plane (along the parallel tank walls or diagonally for the square base basin *or* in the meridional plane for the circular base tank). A *qualitative discrepancy* was only found out for the phase lag (relative to the input harmonic signal) which is, according to the inviscid theories, constant (discrete) values but measurements in [2] do not confirm that fact. The discrepancy was clarified by the *viscous* damping.

The recent experimental studies of the steady-state resonant sloshing in a square base tank [3] showed that the viscous damping, even when being relatively small, may cause nonlinear surface *wave phenomena*, which are *qualitatively* not clarified within the framework of the inviscid hydrodynamic model. In particular, the viscous damping prevents the standing resonant wave to exist for the oblique horizontal tank forcing and it breaks symmetry of the swirling (rotary) wave for the diagonal forcing so that the maximum wave elevations at the two perpendicular walls become non-equal values. Equipping the corresponding Narimanov-Moiseev multimodal equations

(chap. 9 in [1]) with the damping terms, [4] analytically described the surface wave phenomena.

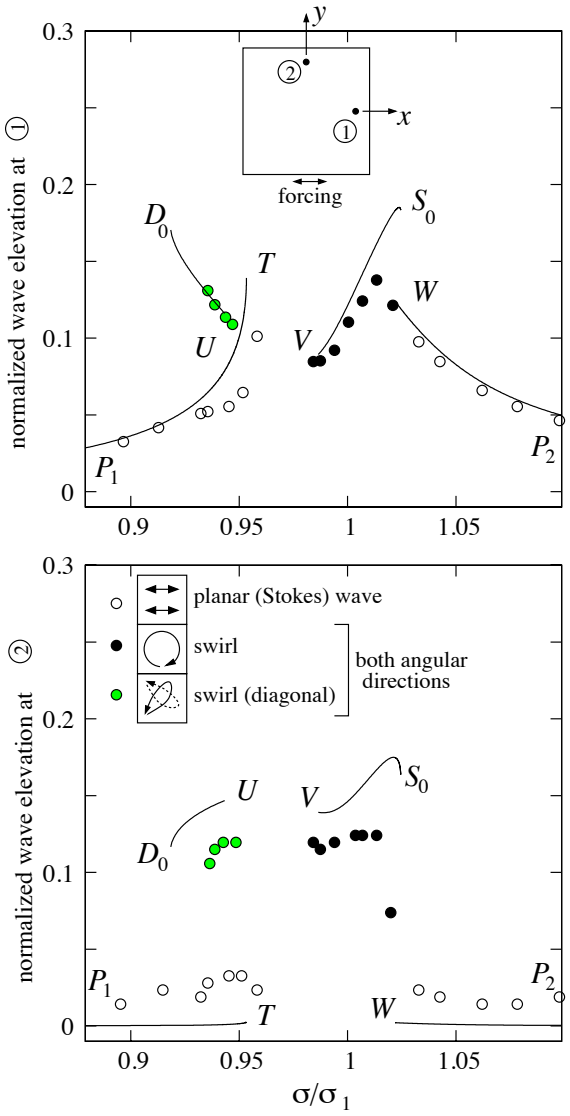

Figure 1. Experimental [3] (symbols) and theoretical [4] (solid lines) normalized maximum wave elevations at two wave probes for the longitudinal harmonic tank forcing of a square base tank. The nondimensional forcing amplitude is equal to 0.00727 and the mean nondimensional liquid depth is $h = 0.6$ (scaled by the tank breadth). The damping rate is taken from the experimental measurements [3]. The empty circles correspond to the experimental planar standing waves. The filled circles imply swirling (both angular wave propagation directions are possible).

Figs. 1-3 present comparisons of experimental measurements [3] and theoretical predictions [4] for three harmonic tank excitation types. The most interesting case (the diagonal forcing) is presented in Fig. 3. Here, the branches $V_1 S_0'$ and $V_2 S_0''$ correspond to the steady-state swirling propagating in the two opposite angular directions. These two branches coincide within the framework of the inviscid potential flow theories (the amplitudes are independent of the wave propagation directions) but [4] mathematically proves that the damping yields the two different branches.

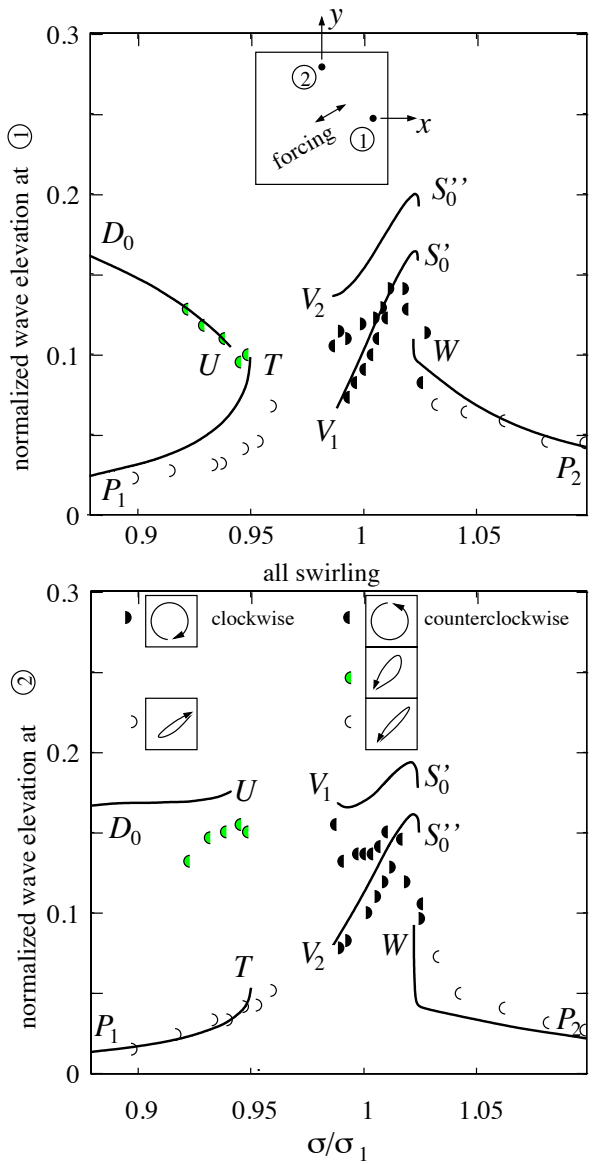

Figure 2. The same as in Fig. 1, but for the oblique harmonic tank excitation with the angle 30^0 relative to Ox -axis. The half-circles (solid) denote the experimentally-detected swirling waves of the corresponding angular direction.

In the spite of a theoretical success in describing the aforementioned nonlinear wave phenomena by accounting for the viscous damping, [4] states a series of open problems. Shortly, these can be formulated as: *What are the actual damping rates, which account for a cumulative effect of diverse energy dissipation phenomena (boundary layer, bulk viscosity, wave breaking, etc.)? What does happen for more complicated three-dimensional forcing types? Can a vortex flow component, if exists, significantly affect the resonant sloshing?*

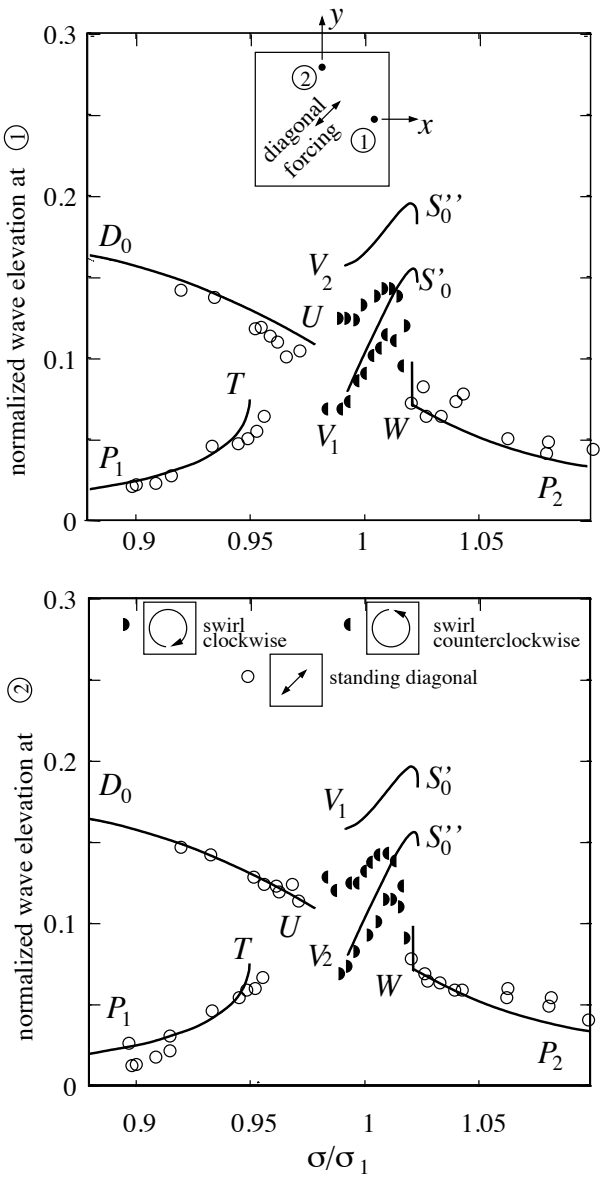

Figure 3. The same as in Fig. 1 but for the diagonal tank forcing. Diagonal standing waves and swirling are possible. The experimental diagonal steady-state waves are marked by the empty circles. In contrast to the undamped case, the steady-state swirling is characterised by an asymmetric amplitude response so that the maximum wave elevations at the two perpendicular tank walls depend on the angular wave-prapagation directions.

Indeed, computations in Figs. 1-3 used the experimentally established damping rates which were 2.56 times larger than their theoretical estimate within the framework of the boundary-layer theory (chap. 6 in [1]). The authors referred to the dynamic contact line effect, which was earlier discussed by Keulegan, to explain this relatively large discrepancy for the experimental tank in [3]. Observations in [2] reported, in addition, a strong wave breaking with free-surface fragmentations as well as the Prandtl steady rotational (vortex) flow [5,6], which occurred during the swirling wave mode. The latter two phenomena can increase the total energy dissipation making it dependent on the resonant wave type and the wave amplitude. Suggesting such an (unknown) dependence helps to explain why agreement between the multimodal theory results [4] and the experimental measurements [3] may significantly be improved by the speculatively-varying damping rates along the response curves.

A special research interest is associated with the resonant sloshing due to the *three-dimensional forcing*. Pioneering theoretical studies on that are reported in [7], where a Narimanov-Moiseev multimodal theory is derived and applied to study the resonant steady-state waves caused by an orbital elliptic motion of an upright annular cylindrical container. Being interested in what happens in bioreactors and, of course, bearing in mind the Prandtl phenomenon [5], the dedicated model tests were made in [8,9] for the circular base tank. These works reported on the strong wave breaking as well as measured and classified the Prandtl steady vortical flow.

The present paper continues [4,7] to gain an insight into the joint effect of the viscous damping and the three-dimensional forcing on the steady-state sloshing in an upright circular cylindical container. The damping terms are introduced in the Narimanov-Moiseev multimodal equations [7] to analytically describe the damped steady-state waves for an arbitrary prescribed periodic sway/surge/pitch/roll tank excitation. The damping rates are not limited to the boundary layer effect [10] but allowed to imply a cumulative dissipation in the mechanical system. We show that the periodic sway/surge/pitch/roll forcing reduces, in the lowest-order approximation, to a horizontal orbital (elliptic) tank excitation. As a consequence, the resonance sloshing types and the response curves may be classified *versus* the ellipse semi-axes ratio (that characterises the focing type) and the damping rates (dissipation).

Existing experiments were done for longitudinal [2] and circular orbital [8,9] tank excitations. These experimental measurements are used to validate and analyse the joint damping-and-the-forcing-type effects. The damping weakly affects the amplitude response for the longitudinal forcing [2] but comparing our analytical theory and the experimental data on the phase lag shows that the damping rate must increase with the wave amplitude to fit the experimental data. An explanation is the wave-breaking related damping. On the other hand, this damping kind is not able to clarify the discrepancy for the orbital forcing [8,9]. The latter means that the forcing type matters. Most probably, the orbital forcing requires to account for the Prandtl phenomenon [5], whose mathematical description needs another hydrodynamic model.

NARIMANOV-MOISEEV MODAL THEORY

Sloshing in an upright circular tank of the radius r_0 is considered in the tank-fixed cylindrical coordinate system. The tank performs a small-amplitude prescribed periodic sway/ surge/roll/pitch motion, which is furthermore described by the r_0-scaled generalised coordinates $\eta_i(t) = O(\varepsilon) \ll 1, i = 1,2,4,5$ shown in Fig. 4. The problem is studied in the nondimensional

statement; r_0 is the characteristic dimension and $1/\sigma$ (σ is the forcing frequency) is the characteristic time.

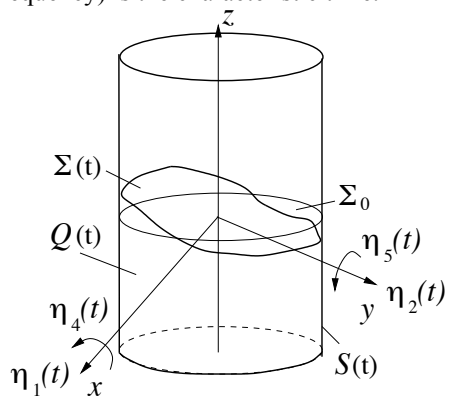

Figure 4. The liquid domain $Q(t)$ is confined by the free surface $\Sigma(t)$ ($\Sigma_0(z=0)$ is the mean liquid plane) and the wetted tank surface $S(t)$. Sloshing is considered in the tank-fixed coordinate system.

The multimodal method [7] employs the natural sloshing modes φ_{Mi} arising from the spectral boundary problem

$$\nabla^2\varphi_{Mi}=0 \ \text{ in } Q_0;\ \ \frac{\partial\varphi_{Mi}}{\partial n}=0 \ \text{ on } S_0,$$
$$\frac{\partial\varphi_{Mi}}{\partial n}=\kappa_{Mi}\varphi_{Mi} \ \text{ on } \Sigma_0;\ \ \int_{\Sigma_0}\varphi_{Mi}\,dS=0, \tag{1}$$

where κ_{Mi} are the eigenvalues, Σ_0 is the mean (unperturbed) free surface, Q_0 is the mean liquid domain, and S_0 is the mean wetted tank surface. For the circular cylindrical tank, the problem (1) has the analytical solution in the cylindrical coordinate system

$$\varphi_{Mi}(r,\theta,z)=\alpha_{Mi}J_M(k_{Mi}r)Z_{Mi}(z)\begin{bmatrix}\sin\\ \cos\end{bmatrix}(M\theta);\ M\ge 0, i>1$$
$$Z_{Mi}(z)=\frac{\cosh(k_{Mi}(z+h))}{\cosh(k_{Mi}h)};\ \ \kappa_{Mi}=k_{Mi}\tanh(k_{Mi}h), \tag{2}$$

where $J'_M(k_{Mi})=0$, h is the nondimensional mean liquid depth, and α_{Mi} are the normalizing coefficients [7]. The dimensional natural sloshing frequencies are computed as

$$\sigma_{Mi}=\sqrt{\kappa_{Mi}\overline{g}};\quad \overline{g}=g/r_0;\quad \overline{\sigma}_{Mi}=\sigma_{Mi}/\sigma, \tag{3}$$

where g is the gravity acceleration.

The natural sloshing modes constitute a complete set of harmonic functions in the mean liquid domain so that the velocity potential can be presented in the form

$$\Phi(r,\theta,z,t)=\dot\eta_1(t)r\cos\theta+\dot\eta_2(t)r\sin\theta + F(r,z)\left[-\dot\eta_4(t)\sin\theta+\dot\eta_5(t)\cos\theta\right] + \sum_{Mi}\alpha_{Mi}J_M(k_{Mi}z)\left[P_{Mi}(t)\cos(M\theta)+R_{mi}(t)\sin(m\theta)\right], \tag{4}$$

where $P_{Mi}(t)$ and $R_{mi}(t)$ are the generalized velocities but the free-surface elevations are posed as

$$z=\zeta(r,\theta,t)=\sum_{Mi}\alpha_{Mi}J_M(k_{Mi}r)\left(p_{Mi}(t)\cos(M\theta)+r_{mi}(t)\sin(m\theta)\right), \tag{5}$$

where $p_{Mi}(t)$ and $r_{mi}(t)$ are the sloshing-related *generalized coordinates*; $\mathrm{F}(r,z)$ comes from the analytically-found (chap. 5 in [1]) Stokes-Joukowski potentials,

$$\mathrm{F}(r,z)=rz-\sum_{n=1}^{\infty}\frac{2P_n}{k_{1n}}J_1(k_{1n}r)\frac{\sinh(k_{1n}(z+\frac{1}{2}h))}{\cosh(\frac{1}{2}k_{1n}h)},$$
$$P_n=\int_0^1 r^2J_1(k_{1n}r)\,\mathrm{d}r. \tag{6}$$

Assuming the forcing frequency σ is close to the lowest natural sloshing frequency $\sigma_1=\sigma_{11}$, $\overline{\sigma}_1\approx 1$ in (3), and there are no secondary resonances, the Narimanov-Moiseev multimodal theory [7] implies that the resonant sloshing response is of the order $O(\varepsilon^{1/3})$ and the dominant contribution is associated with the lowest natural sloshing modes (the generalized coordinates p_{11} and r_{11}). Due to the trigonometric formulas by the angular coordinate, the Narimanov-Moiseev theory requires [7]

$$p_{11}\sim r_{11}=O(\varepsilon^{1/3});\ \ p_{0j}\sim p_{2j}\sim r_{2j}=O(\varepsilon^{2/3}),$$
$$r_{1(j+1)}\sim p_{1(j+1)}\sim r_{3j}\sim p_{3j}=O(\varepsilon),\ j\ge 1; \tag{7}$$

the remaining generalized coordinates are of the order $o(\varepsilon)$. By neglecting the $o(\varepsilon)$- terms, the paper [7] derived the following modal system with respect to p_{Mi} and r_{mi}:

$$\ddot p_{11}+\boxed{2\xi_{11}\overline{\sigma}_{11}\dot p_{11}}+\overline{\sigma}_{11}^2p_{11}+d_1p_{11}\left(\ddot p_{11}p_{11}+\ddot r_{11}r_{11}+\dot p_{11}^2+\dot r_{11}^2\right)$$
$$+d_2\left[r_{11}\left(\ddot p_{11}r_{11}-\ddot r_{11}p_{11}\right)+2\dot r_{11}\left(\dot p_{11}r_{11}-\dot r_{11}p_{11}\right)\right]+\sum_{j=1}^{\infty}\Big[d_3^{(j)}(\ddot p_{11}p_{2j}$$
$$+\ddot r_{11}r_{2j}+\dot p_{11}\dot p_{2j}+\dot r_{11}\dot r_{2j})+d_4^{(j)}(\ddot p_{2j}p_{11}+\ddot r_{2j}r_{11})+d_5^{(j)}(\ddot p_{11}p_{0j}$$
$$+\dot p_{11}\dot p_{0j})+d_6^{(j)}\ddot p_{0j}p_{11}=-(\ddot\eta_1-\overline{g}\eta_5-S_1\ddot\eta_5)\kappa_{11}P_1, \tag{8}$$

$$\ddot r_{11}+\boxed{2\xi_{11}\overline{\sigma}_{11}\dot r_{11}}+\overline{\sigma}_{11}^2r_{11}+d_1r_{11}\left(\ddot p_{11}p_{11}+\ddot r_{11}r_{11}+\dot p_{11}^2+\dot r_{11}^2\right)$$
$$+d_2\left[p_{11}\left(\ddot r_{11}p_{11}-\ddot p_{11}r_{11}\right)+2\dot p_{11}\left(\dot r_{11}p_{11}-\dot p_{11}r_{11}\right)\right]+\sum_{j=1}^{\infty}\Big[d_3^{(j)}(\ddot p_{11}r_{2j}$$
$$-\ddot r_{11}p_{2j}+\dot p_{11}\dot r_{2j}-\dot p_{2j}\dot r_{11}\Big)+d_4^{(j)}(\ddot r_{2j}p_{11}-\ddot p_{2j}r_{11})+d_5^{(j)}(\ddot r_{11}p_{0j}$$
$$+\dot r_{11}\dot p_{0j})+d_6^{(j)}\ddot p_{0j}r_{11}=-(\ddot\eta_2+\overline{g}\eta_4+S_1\ddot\eta_4)\kappa_{11}P_1; \tag{9}$$

$$\ddot p_{2k}+\boxed{2\xi_{2k}\overline{\sigma}_{2k}\dot p_{2k}}+\overline{\sigma}_{2k}^2p_{2k}+d_{7,k}\left(\dot p_{11}^2-\dot r_{11}^2\right)$$
$$+d_{9k}\left(\ddot p_{11}p_{11}-\ddot r_{11}r_{11}\right)=0,\qquad k\ge 1; \tag{10}$$

$$\ddot r_{2k}+\boxed{2\xi_{2k}\overline{\sigma}_{2k}\dot r_{2k}}+\overline{\sigma}_{2k}^2r_{2k}+2d_{7,k}\dot p_{11}\dot r_{11}$$

$$+d_{9,k}\left(\ddot{p}_{11}r_{11}+\ddot{r}_{11}p_{11}\right)=0,\qquad k\geq 1; \tag{11}$$

$$\ddot{p}_{0k}+\boxed{2\xi_{2k}\overline{\sigma}_{2k}\dot{p}_{2k}}+\overline{\sigma}_{0k}^{2}p_{0k}+d_{8,k}\left(\dot{p}_{11}^{2}+\dot{r}_{11}^{2}\right)$$
$$+d_{10,k}\left(\ddot{p}_{11}p_{11}+\ddot{r}_{11}r_{11}\right)=0,\qquad k\geq 1; \tag{12}$$

$$\ddot{p}_{3k}+\boxed{2\xi_{3k}\overline{\sigma}_{3k}\dot{p}_{3k}}+\overline{\sigma}_{3k}^{2}p_{3k}+d_{11,k}\left[\ddot{p}_{11}\left(p_{11}^{2}-r_{11}^{2}\right)-2p_{11}r_{11}\ddot{r}_{11}\right]$$
$$+d_{12,k}\left[p_{11}\left(\dot{p}_{11}^{2}-\dot{r}_{11}^{2}\right)-2r_{11}\dot{p}_{11}\dot{r}_{11}\right]+\sum_{j=1}^{\infty}\left[d_{13,k}^{(j)}\left(\ddot{p}_{11}p_{2j}-\ddot{r}_{11}r_{2j}\right)\right.$$
$$\left.+d_{14,k}^{(j)}\left(\ddot{p}_{2j}p_{11}-\ddot{r}_{2j}r_{11}\right)+d_{15,k}^{(j)}\left(\dot{p}_{2j}p_{11}-\dot{r}_{2j}r_{11}\right)=0,\quad k\geq 1, \right. \tag{13}$$

$$\ddot{r}_{3k}+\boxed{2\xi_{3k}\overline{\sigma}_{3k}\dot{r}_{3k}}+\overline{\sigma}_{3k}^{2}r_{3k}+d_{11,k}\left[\ddot{r}_{11}\left(p_{11}^{2}-r_{11}^{2}\right)+2p_{11}r_{11}\ddot{p}_{11}\right]$$
$$+d_{12,k}\left[r_{11}\left(\dot{p}_{11}^{2}-\dot{r}_{11}^{2}\right)+2p_{11}\dot{p}_{11}\dot{r}_{11}\right]+\sum_{j=1}^{\infty}\left[d_{13,k}^{(j)}\left(\ddot{p}_{11}r_{2j}+\ddot{r}_{11}p_{2j}\right)\right.$$
$$\left.+d_{14,k}^{(j)}\left(\ddot{p}_{2j}r_{11}+\ddot{r}_{2j}p_{11}\right)+d_{15,k}^{(j)}\left(\dot{p}_{2j}\dot{r}_{11}+\dot{r}_{2j}\dot{p}_{11}\right)\right]=0,\qquad k\geq 1; \tag{14}$$

$$\ddot{p}_{1n}+\boxed{2\xi_{1n}\overline{\sigma}_{1n}\dot{p}_{1n}}+\overline{\sigma}_{1n}^{2}p_{1n}+d_{16,n}\left(\ddot{p}_{11}p_{11}^{2}+r_{11}p_{11}\ddot{r}_{11}\right)+d_{17,n}\left(\ddot{p}_{11}r_{11}^{2}\right.$$
$$\left.-r_{11}p_{11}\ddot{r}_{11}\right)+d_{18,n}p_{11}\left(\dot{p}_{11}^{2}+\dot{r}_{11}^{2}\right)+d_{19,n}\left(r_{11}\dot{p}_{11}\dot{r}_{11}-p_{11}\dot{r}_{11}^{2}\right)$$
$$+\sum_{j=1}^{\infty}\left[d_{20,n}^{(j)}\left(\ddot{p}_{11}p_{2j}+\ddot{r}_{11}r_{2j}\right)+d_{21,n}^{(j)}\left(p_{11}\ddot{p}_{2j}+\ddot{r}_{11}r_{2j}\right)\right.$$
$$\left.+d_{22,n}^{(j)}\left(\dot{p}_{11}\dot{p}_{2j}+\dot{r}_{11}r_{2j}\right)+d_{23,n}^{(j)}\ddot{p}_{11}p_{0j}+d_{24,n}^{(j)}p_{11}\ddot{p}_{0j}+d_{25,n}^{(j)}\dot{p}_{11}\dot{p}_{0j}\right]$$
$$=-(\ddot{\eta}_{1}-\overline{g}\eta_{5}-S_{n}\ddot{\eta}_{5})\kappa_{1n}P_{n},\qquad n\geq 2, \tag{15}$$

$$\ddot{r}_{1n}+\boxed{2\xi_{1n}\overline{\sigma}_{1n}\dot{r}_{1n}}+\sigma_{1n}^{2}r_{1n}+d_{16,n}\left(\ddot{r}_{11}r_{11}^{2}+r_{11}p_{11}\ddot{p}_{11}\right)+d_{17,n}\left(\ddot{r}_{11}p_{11}^{2}\right.$$
$$\left.-r_{11}p_{11}\ddot{p}_{11}\right)+d_{18,n}r_{11}\left(\dot{p}_{11}^{2}+\dot{r}_{11}^{2}\right)+d_{19,n}\left(p_{11}\dot{p}_{11}\dot{r}_{11}-r_{11}\dot{p}_{11}^{2}\right)$$
$$+\sum_{j=1}^{\infty}\left[d_{20,n}^{(j)}\left(\ddot{p}_{11}p_{2j}-\ddot{r}_{11}p_{2j}\right)+d_{21,n}^{(j)}\left(p_{11}\ddot{r}_{2j}-r_{11}\ddot{p}_{2j}\right)\right.$$
$$\left.+d_{22,n}^{(j)}\left(\dot{p}_{11}\dot{r}_{2j}-\dot{r}_{11}\dot{p}_{2j}\right)+d_{23,n}^{(j)}\ddot{r}_{11}p_{0j}+d_{24,n}^{(j)}r_{11}\ddot{p}_{0j}+d_{25,n}^{(j)}\dot{r}_{11}\dot{p}_{0j}\right]$$
$$=-(\ddot{\eta}_{2}+\overline{g}\eta_{4}+S_{n}\ddot{\eta}_{4})\kappa_{1n}P_{n},\qquad n\geq 2, \tag{16}$$

which, within to the $o(\varepsilon)$ quantities, describes the resonant nonlinear sloshing. The hydrodynamic coefficients at the nonlinear quantities were found explicitly and computed as functions of h [7].

A novelty is the framed damping terms, which were absent in the original work [7]. We assume that the damping rates ξ_{Mi} express a *cumulative effect* of different *dissipative* factors whose lower bound is associated with the linear boundary layer and bulk damping effects. This means that $\xi_{Mi}\geq\xi_{Mi}^{low}$, where, according to [10],

$$\xi_{Mi}^{low}=\xi_{Mi}^{bl}+\xi_{Mi}^{bu}, \tag{17}$$
$$\xi_{Mi}^{bu}=\delta^{2}\left[\frac{2k_{Mi}^{2}}{\kappa_{Mi}^{1/2}}-\frac{\mu_{Mi}^{(2)}J_{M}^{2}(k_{Mi})}{2\kappa_{Mi}^{3/2}\mu_{Mi}^{(0)}}\right],$$
$$\xi_{Mi}^{bl}=\delta\frac{\mu_{Mi}^{(1)}+\frac{1}{2}J_{M}^{2}(k_{Mi})(\mu_{Mi}^{(2)}+\mu_{Mi}^{(3)})}{2\sqrt{2}\ \kappa_{Mi}^{5/4}\mu_{Mi}^{(0)}},$$

in which

$$\mu_{Mi}^{(0)}=\int_{0}^{1}rJ_{M}^{2}(k_{Mi}r)\,\mathrm{d}r,$$
$$\mu_{Mi}^{(1)}=\int_{0}^{1}rk_{Mi}^{2}J_{M}'^{2}(k_{Mi}r)\,\mathrm{d}r+M^{2}\int_{0}^{1}\frac{J_{M}^{2}(k_{Mi}r)}{r}\mathrm{d}r,$$
$$\mu_{Mi}^{(2)}=M^{2}\left(\frac{\tanh(k_{Mi}h)}{k_{Mi}}+\frac{h}{\cosh^{2}(k_{Mi}h)}\right),$$
$$\mu_{Mi}^{(3)}=k_{Mi}^{2}\left(\frac{\tanh(k_{Mi}h)}{k_{Mi}}-\frac{h}{\cosh^{2}(k_{Mi}h)}\right),$$
$$\delta=\mathrm{Ga}^{-1/4}=\sqrt{\nu/(g^{1/2}R_{0}^{3/2})}\ll 1 \tag{18}$$

(Ga is the Galilei number, δ implies the nondimensional boundary layer thickness at the wetted tank surface).

Inserting the linear damping terms into the modal equations (8)-(16), which was derived from the inviscid potential flow hydrodynamic model, implicitly assumes that the actual damping coefficients are small values on the $\varepsilon^{1/3}$-scale.

STEADY-STATE ASYMPTOTIC SOLUTION

The third-order generalized coordinates, which are governed by (13)-(16), are `driven' so that, as long as we know a steady-state (periodic) solution of (8)-(12), in which only the first two equations have inhomogeneous right-hand sides, one can analytically get the third-order contribution by (13)-(16). Substituting the time-periodic Fourier representation of $\eta_{i}(t)$ into the first two equations of (8), (9) and gathering the main harmonics lead to $\left[\varepsilon_{x}\cos t+\overline{\varepsilon}_{x}\sin t+\text{higher harmonics}\right]$ and $\left[\overline{\varepsilon}_{y}\cos t+\varepsilon_{y}\sin t+\text{higher harmonics}\right]$ in the right-hand sides of (8) and (9), respectively. The same lowest-order Fourier harmonics appear for the horizontal *elliptical tank motions*. The elliptic trajectory reduces to its canonic form and, therefore, without loss of generality, focusing on the counterclockwise forcing direction and superposing the major semi-axis of the ellipse with Ox lead to

$$\varepsilon_{x}>0,\quad 0\leq\varepsilon_{y}=\gamma\varepsilon_{x}\leq\varepsilon_{x},\quad \overline{\varepsilon}_{x}=\overline{\varepsilon}_{y}=0. \tag{19}$$

Henceforth, we restrict ourselves to (19) and treat the sway/roll/pitch/surge tank excitation types by the single nondimensional parameter $0\leq\gamma\leq 1$ (the ellipse semi-axes ratio), where the limit cases $\gamma=0$ and 1 imply longitudinal and rotary (circular) tank excitations, respectively.

To find an asymptotic periodic solution of (8)-(16), we pose the lowest-order quantities as

$$\begin{aligned}p_{11}&=a\cos(\sigma t)+\overline{a}\sin(\sigma t)+O(\varepsilon),\\ r_{11}&=\overline{b}\cos(\sigma t)+b\sin(\sigma t)+O(\varepsilon),\end{aligned} \tag{20}$$

where $a, \overline{a}, b$, and $\overline{b}$ are the nondimensional amplitude parameters of the order $O(\varepsilon^{1/3})$. Inserting (20) into (10)-(12) makes it possible to find explicit asymptotic expressions for the $O(\varepsilon^{2/3})$-generalized coordinates p_{0k}, p_{2k}, and r_{2k}. Obviously, the damping terms in the corresponding modal equations can be neglected as giving a small contribution for the non-resonant behavior by p_{0k}, p_{2k}, and r_{2k}. Substituting (20), p_{0k}, p_{2k}, r_{2k} into (8), (9) and gathering the first Fourier harmonics lead to the *secular* system of nonlinear algebraic equations

$$\begin{aligned}
&a\left[\Lambda + m_1\left(a^2 + \overline{a}^2 + \overline{b}^2\right) + m_3 b^2\right] + \overline{a}(m_2 b\overline{b} + \xi) = \varepsilon_x,\\
&\overline{a}\left[\Lambda + m_1\left(a^2 + \overline{a}^2 + b^2\right) + m_3 \overline{b}^2\right] + a(m_2 b\overline{b} - \xi) = 0,\\
&\overline{b}\left[\Lambda + m_1\left(a^2 + b^2 + \overline{b}^2\right) + m_3 \overline{a}^2\right] + b(m_2 \overline{a}a + \xi) = \varepsilon_y,\\
&b\left[\Lambda + m_1\left(b^2 + \overline{a}^2 + \overline{b}^2\right) + m_3 a^2\right] + \overline{b}(m_2 \overline{a}a - \xi) = 0,
\end{aligned} \tag{21}$$

where $\Lambda = \overline{\sigma}_{11}^2 - 1$, $m_2 = m_1 - m_3$, $\xi = 2\xi_{11}$, and m_i are the analytically-known functions of the hydrodynamic coefficients. Having known the lowest-order amplitude parameters from (21) makes it possible to study the stability of the steady-state solution by using the multi-timing scheme and the linear Lyapunov method [4].

Following [7] shows that the constructed asymptotic solution predicts, by neglecting the higher-order terms, either *standing* or *swirling* wave modes. Indeed, according to (20), the steady-state sloshing is approximated by

$$\begin{aligned}
\zeta(r,\theta,t) = J_1(k_{11}r)\big[&(a\cos\theta + \overline{b}\sin\theta)\cos t\\
&+ (\overline{a}\cos\theta + b\sin\theta)\sin t\big] + o(\varepsilon^{1/3}),
\end{aligned} \tag{22}$$

which always determines swirling unless $ab = \overline{a}\overline{b}$ when a standing wave is expected.

For the undamped case with $\xi = 0$, [7] mathematically proved that $\overline{a} = \overline{b} = 0$ as $0 \le \gamma < 1$. This is *not* true for the damped case, physically, due to the non-constant phase lags. We introduce the integral amplitudes and the phase lags

$$a = A\cos\psi,\ \overline{a} = A\sin\psi,\ \overline{b} = B\cos\varphi,\ b = B\sin\varphi \tag{23}$$

and re-write (21) in the form

$$\begin{aligned}
&A\left[\Lambda + m_1 A^2 + (m_3 - F)B^2\right] = \varepsilon_x\cos\psi,\\
&B\left[\Lambda + m_1 B^2 + (m_3 - F)A^2\right] = \varepsilon_y\sin\varphi,\\
&A\left[DB^2 + \xi\right] = \varepsilon_x\sin\psi,\quad B\left[DA^2 - \xi\right] = \varepsilon_y\cos\varphi,
\end{aligned} \tag{24}$$

where

$$\begin{aligned}
&F = -m_2\cos^2\alpha = -m_2/(1+C^2),\ \alpha = \varphi - \psi\\
&D = -m_2\sin\alpha\cos\alpha = -m_2 C/(1+C^2),\ C = \tan\alpha.
\end{aligned} \tag{25}$$

LONGITUDINAL FORCING

For the longitudinal forcing along the Ox-axis ($\gamma = 0$), the undamped sloshing implies either planar standing waves $A > 0,\ B = 0,\ \sin\psi = 0$ (the phase lag φ has no meaning) or swirling with $AB > 0,\ \sin\psi = \cos\varphi = 0,\ (C = \pm\infty)$. The swirling wave mode corresponds to the two physically identical angularly propagating waves, where the counterclockwise direction corresponds to $C = +\infty$ and the clockwise one to $C = -\infty$.

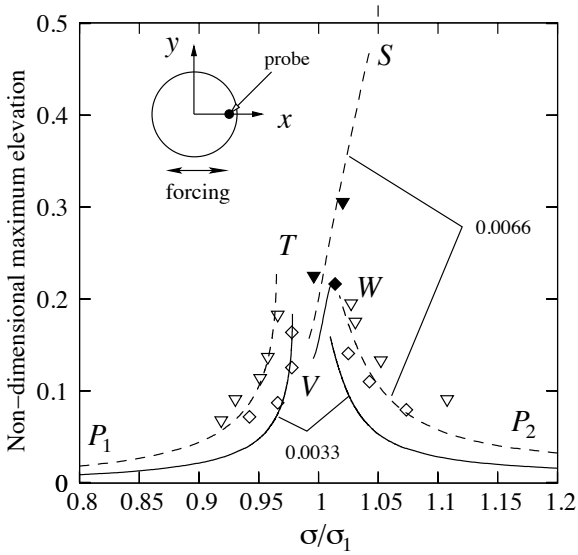

Figure 5. Theoretical (solid and dashed lines) and experimental (symbols) nondimensional maximum wave elevations at the wave probe $(0.75R_0, 0)$ for the longitudinal forcing amplitudes $\eta_{a1} = 0.0033$ and 0.0066; computations adopted $\xi = 0.0128$ in (24). The empty symbols imply the experimental planar standing waves but the filled symbols correspond to the swirling wave mode.

When the viscous damping matters ($\xi > 0$), (24) determines, physically, the same solution types. For the planar wave, the non-zero amplitude A and phase lag ψ come from

$$\begin{aligned}
&A^2\left[\left(\Lambda + m_1 A^2\right)^2 + \xi^2\right] = \varepsilon_x^2,\quad 0 < A \le \varepsilon_x/\xi,\\
&\psi = \arccos\left(A\left(\Lambda + m_1 A^2\right)/\varepsilon_x\right).
\end{aligned} \tag{26}$$

To describe swirling, one should solve the cubic equation $q_3 C^3 + q_2 C^2 + q_1 C + q_0 = 0$, where $q_3 = \xi^2(m_1 + m_3)^2 > 0$, $q_2 = 2\xi^2\Lambda(m_3^2 - m_1^2)$, $q_1 = \xi\left[4\xi^2 m_1^2 + \Lambda^2 m_2^2\right]$, $q_0 = \varepsilon_x^2 m_1^2 m_2$, whose roots, being substituted into

$$\begin{aligned}
&A^2 = \frac{\xi(1+C^2)}{(m_3 - m_1)C} > 0,\\
&B^2 = -\frac{1}{m_1}\left[\Lambda + \frac{m_1 + m_3 C^2}{1+C^2}A^2\right] > 0
\end{aligned} \tag{27}$$

return the wave amplitudes but, continuing with

$$\cos\psi = \frac{A}{\varepsilon_x}\left[\Lambda + m_1 A^2 + \frac{m_1 + m_3 C^2}{1+C^2} B^2\right],$$
$$\sin\psi = \frac{A}{\varepsilon_x}\left[\xi + \frac{(m_3 - m_1)C}{1+C^2} B^2\right] \quad (28)$$

give the phase lag ψ; another phase lag φ is determined by

$$\varphi_1 = \psi + \arctan C, \quad \varphi_2 = \varphi_1 \pm \pi, \quad (29)$$

($\pm$ means the two physically-identical angular progressive waves occurring in the two opposite angular directions).

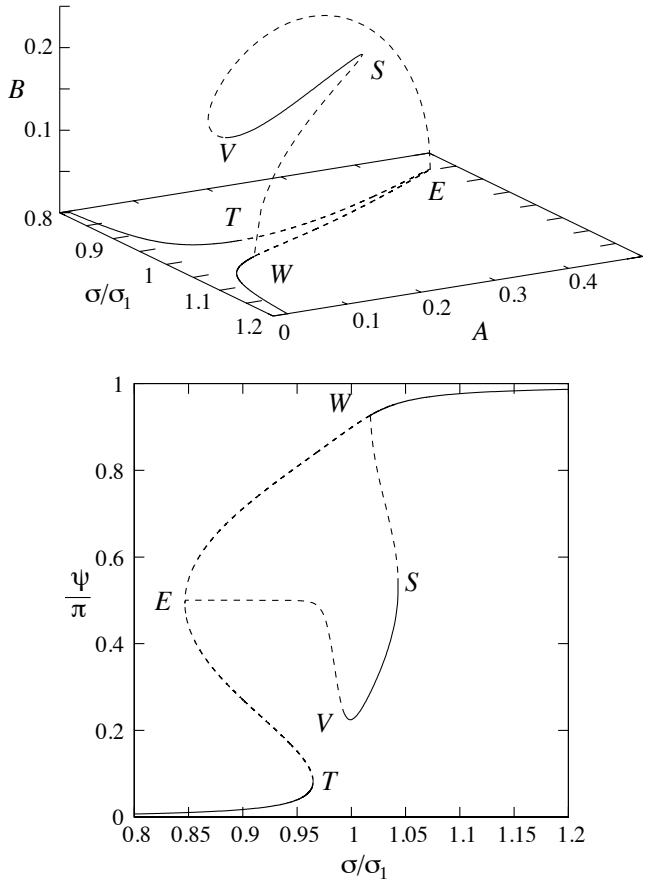

Figure 6. Theoretical amplitude parameters A, B (top) and the phase lag ψ (bottom) *versus* the forcing frequency σ / σ_1. The case is associated with one experimental series in [2] when the longitudinal forcing amplitude was equal to $\eta_{1a} = 0.0066$ ($h = 1.5$). The computations adopted the damping coefficient $\xi = 0.0128$.

Using the derived steady-state solution and formulas in appendix of [7], theoretical predictions of the maximum wave elevations at the walls can be computed and compared with the experimental measurements in [2] done with the relatively small forcing amplitude. Fig. 5 shows that the results are in a satisfactory agreement and the only difference from analogous comparison for the undamped sloshing in [7] is a new point S, which determines the upper limit for the swirling wave mode. The theoretical value of $\xi = 2\xi_{11}^{low}$ by (17)-(18) is 0.005. However, computations in Fig. 5 adopted $\xi = 0.0128 = 0.005 \cdot 2.56$. Why this larger value is used will be explained below. Generally speaking, our numerical tests with $0.005 \le \xi \le 0.0128$ showed that these values of the damping coefficient weakly affect the maximum wave elevations in Fig. 5 but it significantly influences position of the point S.

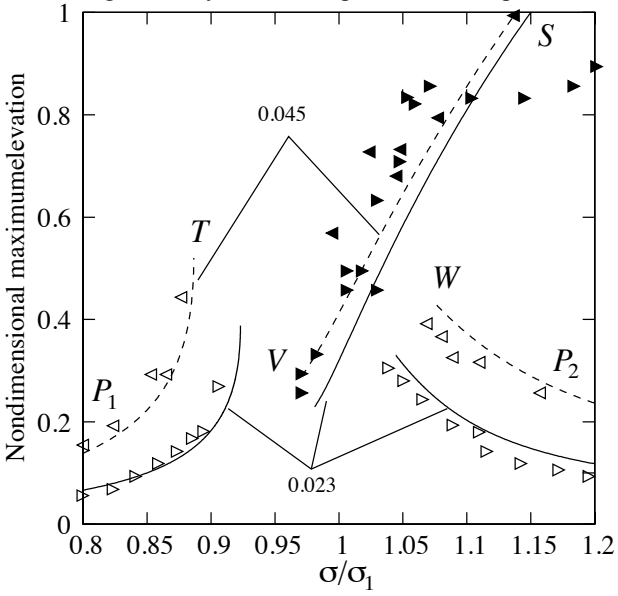

Figure 7. The same as in Fig. 5 but for $\eta_{a1} = 0.023$ and 0.045.

The steady-state response curves, the lowest-order amplitude parameters A, B and the phase lag ψ versus the forcing frequency, are presented in Fig. 6 for the second experimental case in Fig. 5 ($\eta_{1a} = 0.0066$ and $\xi = 0.0128$ in computations). The solid lines mark the stable steady-state solution but the dashed lines imply the hydrodynamic instability. The end points of the stable branches adopt notations from Fig. 5. A focus is on the second panel in Fig. 6, where we demonstrate the phase lag ψ versus σ / σ_1. As we mentioned above, the undamped sloshing is characterized by discrete values of ψ but this panel shows that the phase lag ψ continuously changes between 0 and π.

The calculations in Figs. 5-6 were done with $\xi = 0.0128$. The damping coefficient is much larger than the lower bound $\xi = 2\xi_{11}^{low} = 0.005$ by (17)-(18). Because the wave amplitudes weakly depend on ξ, the actual values of ξ should be estimated from the experimental data by using either the S position or, even better, the phase lag ψ behavior. The latter behavior was measured and reported in [2] for the forcing amplitude $\eta_{1a} = 0.045$. Figs. 7 and 8 compare the theoretical and experimental maximum wave elevations and the phase lag,

respectively, for this experimental case. One can see a satisfactory agreement with our theory in Fig. 7 for the maximum wave elevation where a discrepancy increases only nearby of S, which should be theoretically located far away from the experimentally detected values of σ/σ_1 (experiments do not confirm that).

The experimental data for ψ are presented in Fig. 8, where the theoretical curves were also drawn being computed with different values of ξ. One can see that the theoretical ξ should increase with increasing the wave amplitude response (from V to S) to fit the measured phase lag. This increase may be explained by the strong wave breaking, which is reported in [2]. The minimum experimental value of $\xi = 0.0128$ is extrapolated in Fig. 8 at the primary resonance $\sigma/\sigma_1 = 1$. This minimum value was therefore adopted in our calculations for the experimental tank in [2].

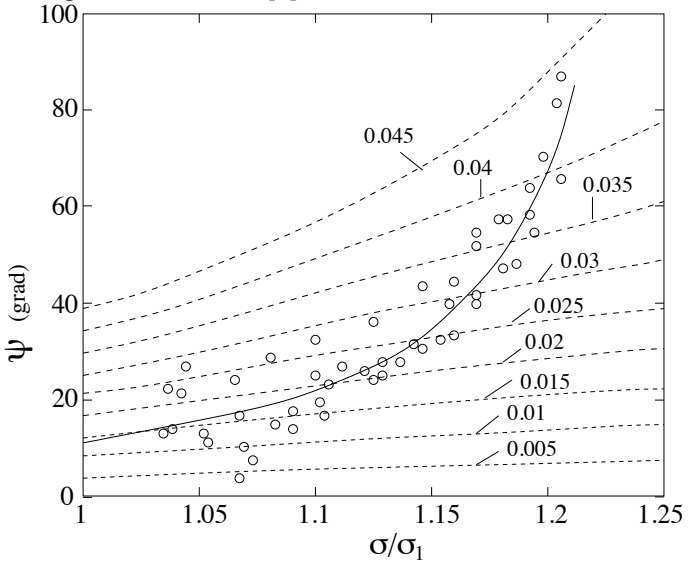

Figure 8. Experimental values of the phase lag ψ (circles) for the stable swirling (subbranch VS in Figs. 6 and 7) are compared with their theoretical estimates for different ξ (dashed lines are marked by the ξ values); $h = 1.5$ and the horizontal longitudinal harmonic forcing amplitude is $\eta_{1a} = 0.045$. The solid line demonstrates the mean-square approximation curve of the experimental data. The comparison shows that the damping coefficient must increase with increasing the wave amplitude.

ELLIPTIC TANK EXCITATIONS

According to [7], the undamped steady-state sloshing is characterized by $\overline{a} = \overline{b} = 0$ in (21), which automatically implies that the phase lags hold discrete values satisfying $\sin\psi = \cos\varphi = 0$ and $\cos\alpha = 0,\ \sin\alpha = \pm 1$. In contrast to that, if $\xi > 0$, the phase lags become complicated functions of the input parameters to be found from (24). Following [4] rewrites (24) in the form

$$A^2\left[\left(\Lambda + m_1A^2 + (m_3 - F)B^2\right)^2 + \left(DB^2 + \xi\right)^2\right] = \varepsilon_x^2,$$
$$B^2\left[\left(\Lambda + m_1B^2 + (m_3 - F)A^2\right)^2 + \left(DA^2 - \xi\right)^2\right] = \varepsilon_y^2, \qquad (30)$$
$$\xi\left(A^2 - B^2\right)D + \frac{F\left[\xi^2 + \left(\Lambda + m_1(A^2 + B^2)\right)^2\right]}{m_2} = -D^2A^2B^2,$$

where F and D are functions of C by (25).

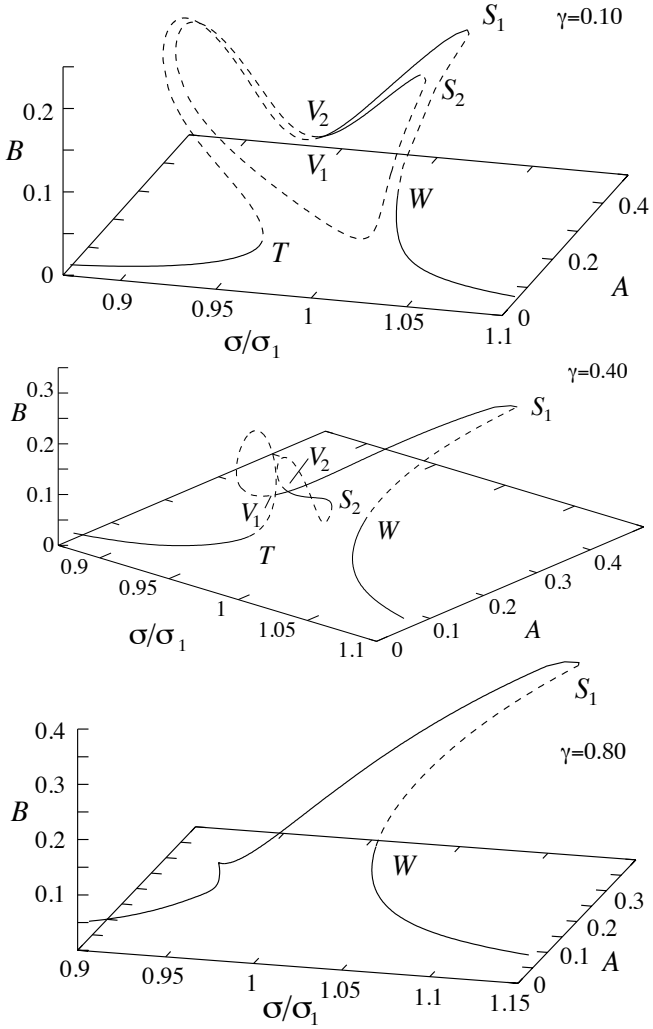

Figure 9. The amplitude response curves in the $(\sigma/\sigma_1, A, B)$-space for three different values of γ, which illustrate a passage from the longitudinal ($\gamma = 0$, Fig. 6) forcing to the circular orbital forcing ($\gamma = 1$, Fig. 10). The solid lines denote the stability but the dashed ones mark the unstable sloshing. All points on these branches imply the swirling wave mode. The branch with T, V_1, S_1, W corresponds to the co-directed (with the elliptic forcing) swirling but V_2S_2 implies the counter-directed one.

Fig. 9 shows the amplitude response curves in the $(\sigma/\sigma_1, A, B)$ space for three different values of γ when $h=1.5$, $\xi=0.0128$, and $\eta_{1a}=0.0066$. Comparing the top pictures in Figs. 5 and 9 shows that passaging from the longitudinal ($\gamma=0$) to elliptic excitations with a relatively-small minor semi-axis ($\gamma=0.10$) splits the $TE(V,S)W$ branch in Fig. 5 into two non-connected branches: the first branch TV_1S_1W implies the co-directed (with the elliptic forcing) swirling but the second one, V_2S_2, (has a loop-like shape) corresponds to the counter-directed swirling. For small γ, there exists the frequency range between T and V_1 where irregular waves (chaos) are expected. This is the same as for the longitudinal forcing (between T and V) in Fig. 5.

Increasing γ (a passage to the rotary tank forcing) makes the branch V_2S_2 and the chaos disappearing so that the counter-directed swirling becomes impossible starting from a certain value of γ and the stable co-directed swirling wave always exists in the primary resonance zone. Furthermore, when γ tends to 1 (see, the bottom picture in Fig. 9 with $\gamma=0.80$), the two amplitude parameters become nearly equal, $A\approx B$.

ROTARY TANK EXCITATION

For the undamped sloshing [7], the rotary orbital forcing may cause the steady-state swirling to propagate in both angular directions. As we showed above, this does not happen when $\xi\neq 0$. To study this case, $\varepsilon=\varepsilon_x=\varepsilon_y$, we recall that $C\neq 0$ but the limit case $C=+\infty,\ A=B$ is possible. The last equation of (30) becomes then an identity but the remaining equations reduce to ($F=D=0$)

$$A^2\left[\left(\Lambda+(m_1+m_3)A^2\right)^2+\xi^2\right]=\varepsilon^2;\quad A=B>0, \qquad (31)$$

$\varphi=\psi+\pi/2$, where ψ comes from

$$A\left[\Lambda+(m_1+m_3)A^2\right]=\varepsilon\cos\psi;\quad A\xi=\varepsilon\sin\psi. \qquad (32)$$

Calculations show that the parameters m_1 and m_3 satisfy the inequalities $m_1<0, m_3>0$ and $m_1+m_3>0$ as $h>1$ so that the response curves following from (31) should possess the hard-spring type behavior. The typical response curve is illustrated in Fig. 10. The frequency ratio $\left(\sigma/\sigma_1\right)_*$ of the point S_* (located between W and S_1) is determined by the inequality

$$1<\left(\sigma/\sigma_1\right)_*\le\left\{1-(m_1+m_3)\left(\varepsilon/\xi\right)^2\right\}^{-1/2}. \qquad (33)$$

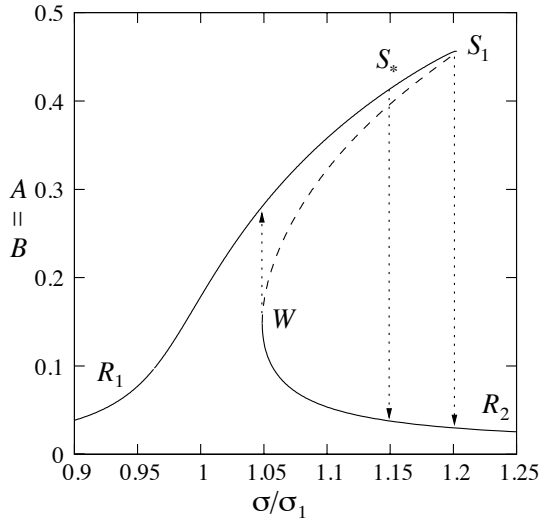

Figure 10. Typical theoretical response curves for the rotary orbital tank excitation. The solid lines imply the stability but the dashed lines mark the unstable steady-state sloshing. There is a hysteresis between W and S_1 where two steady-state solutions co-exist. Position of S_1 is fully determined by the damping coefficient ξ. The calculations were made with $\eta_{1a}=\eta_{2a}=0.0066$, $h=1.5$ and $\xi=0.0128$.

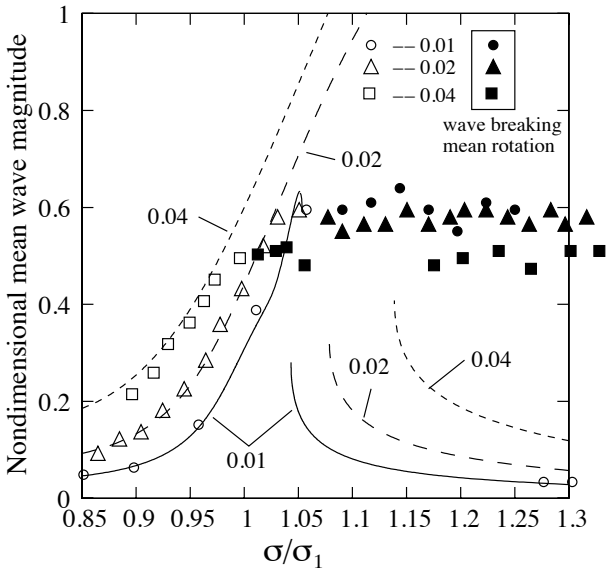

Figure 11. Theoretical (lines) and experimental (symbols) nondimensional wave magnitude $(\zeta_{\max}-\zeta_{\min})/2$ for the rotary orbital tank forcing. The experiments [8,9] were done with a stepwise increase of σ providing a path-following along the upper branch in Fig. 10. The theoretical curves are marked by the nondimensional forcing amplitudes $\eta_{1a}=\eta_{2a}=$ 0.01, 0.02, and 0.04; the computations adopt $\xi=0.034$. The filled symbols mark the experimental observations detecting both the strong wave breaking phenomenon and the steady liquid rotation (the Prandtl phenomenon [5,6]).

The upper limit in (33) increases with ε/ξ so that having known ξ makes it possible to evaluate S_1, where a jump from the upper to lower branch must occur with increasing the forcing frequency σ. Using a stepwise procedure by σ, which provides a path-following along R_1S_1 in Fig. 10, [8,9] conducted model tests with two different tanks of the radii 72 and 287 mm filled with the nondimensional liquid depth 1.04. Various forcing amplitudes and frequencies were tested. Our asymptotic theory requires relatively small forcing amplitude and σ should be in a neighborhood of the primary resonance σ_1. Three model test runs in [8,9] were done with $\eta_{1a}=\eta_{2a}=0.01$, 0.02 and 0.04, for which the constructed theory should, generally, be applicable.

The formulas (17)-(18) estimate the lower bound $\xi \geq \xi_{11}^{low}=0.031$ for the experimental tank filled with a tap water. Using the experimentally established frequencies where a jump from the upper to lower branch occurs (associated with the point S_1 in Fig. 10) and the formula (33) estimates the upper bound for the damping coefficient $\xi \leq 0.034$ (for the lower forcing amplitudes 0.01 and 0.02, $(\sigma/\sigma_1)_*=1.27$ and 1.45, respectively). This means that the viscous damping in [8,9] was relatively small and it is basically associated with the boundary layer at the wetted tank surface.

Using $\xi=0.034$ in our formulas makes it possible to compare our theoretical estimates with the experimental results [8,9]. Fig. 11 demonstrates a good agreement in the frequency ranges where the experimental observations did not detect the wave breaking. However, a significant discrepancy is detected for the filled symbols (the wave breaking occurs). Even though the wave breaking effect may in many cases be modeled by including a larger damping coefficient (as for the longitudinal forcing in [2]), since $\xi \leq 0.034$, getting a better agreement by increasing ξ is theoretically impossible for the cases in Fig. 11. Dedicated numerical tests confirmed that point. Most probably, the discrepancy is due to the steady Prandtl liquid rotation, which was also observed and measured in [8,9].

CONCLUSIONS

Recent experimental studies showed that the *viscous* damping may *qualitatively* affect resonant sloshing in clean tanks, which are exposed to a prescribed periodic motion with the forcing frequency close to the lowest natural sloshing frequency. Some of the corresponding surface-wave phenomena [3] were successfully described in [4] for an obliquely forced square base tank. A modified Narimanov-Moiseev multimodal theory was used.

Adopting analogous modifications in the modal theory for an upright circular tank [7] and using experimental results [2,8,9], we study effect of both the viscous damping and the three-dimensional forcing type (after showing that any small-amplitude sway/roll/pitch/surge periodic motion reduces in the lowest approximation to an elliptic orbital forcing) on the steady-state resonant sloshing.

We show that that the damping significantly influences the phase lag and the cumulative damping in the mechanical system may depend on the steady-state wave amplitude caused by various free-surface phenomena. Furthermore, we prove that the damping, even being small, makes impossible the counter-directed (to the forcing direction) swirling wave for the orbital circular tank forcing. The latter forcing was used in experiments [8,9]. The constructed analytical predictions are supported by these experiments when there is no wave breaking observed in [8,9]. Whereas the wave breaking effect can be accounted for by an increase of the damping rate for the longitudinal forcing [2], this is not possible for the orbital tank excitations. To clarify the appearing discrepancy for this forcing type, one should most probably account for the steady vortex liquid rotation (Prandtl's phenomenon [5]) extensively measured and discussed in [8,9]. An analytical approach to handle the phenomenon is a challenge.

REFERENCES

[1] Faltinsen, O.M. and Timokha, A.N., 2009, *Sloshing*, Cambridge University Press.

[2] Royon-Lebeaud, A., Hopfinger, E.J. and Cartellier, A., 2007, "Liquid sloshing and wave breaking in circular and square-base cylindrical containers", *Journal of Fluid Mechanics*, Vol. **577**, pp. 467–494.

[3] Ikeda, T., Ibrahim, R.A., Harata, Y. and Kuriyama, T., 2012, "Nonlinear liquid sloshing in a square tank subjected to oblique horizontal excitaion", *Journal of Fluid Mechanics*, Vol. **700**, pp. 304-328.

[4] Faltinsen, O.M. and Timokha, A.N., 2017, "Resonant three-dimensional nonlinear sloshing in a square-base basin. Part 4. Oblique forcing and linear damping", *Journal of Fluid Mechanics*, Vol. **822**, pp. 139–169.

[5] Prandtl, L., 1949, "Erzeugung von Zirkulation beim Schütteln von Gefässen", *ZAMM*, Vol. 29, pp. 8-9.

[6] Hutton, R.E., 1964, "Fluid-particle during rotary sloshing", *Journal of Applied Mechanics, Transactions ASME*, Vol. **31**, pp. 145-153.

[7] Faltinsen, O.M., Lukovsky, I.A. and Timokha, A.N., 2016, "Resonant sloshing in an upright annular tank", *Journal of Fluid Mechanics*, Vol. **804**, pp. 608-645.

[8] Reclari, M., Dreyer, M., Tissot, S., Obreschjow, D., Wurm, F.M., 2014, "Surface wave dynamics in orbital shaken cylindrical containers", *Physics of Fluids*, Vol. 26, 052104.

[9] Reclari, M., 2013, "Hydrodynamics of orbital shaken bioreactors", *PhD Thesis # 5759, Laboratoire de Machines Hydrauliques, Ecole Polytechnique Federale de Lausanne*, 159 p.

[10] Miles, J.W. and Henderson, D.M., 1998, "A note on interior vs. boundary-layer damping if surface waves in a circular tank", *Journal of Fluid Mechanics*, Vol. **364**, pp. 319–323.

